Check for updates

Low temperature ensures FeS_2 cathode a superior cycling stability in $Li_7P_3S_{11}$-based all-solid-state lithium batteries

Ru Wang[1†], Zhongkai Wu[1†], Chuang Yu[1]*, Chaochao Wei[1], Linfeng Peng[1], Liping Wang[2]*, Shijie Cheng[1] and Jia Xie[1]*

[1]State Key Laboratory of Advanced Electromagnetic Engineering and Technology, School of Electrical and Electronic Engineering, Huazhong University of Science and Technology, Wuhan, China, [2]School of Materials and Energy, University of Electronic Science and Technology of China, Chengdu, China

All-solid-state lithium sulfide batteries exhibit great potential as next-generation energy storage devices due to their low cost and high energy density. However, the poor conductivity of the solid electrolytes and the low electronic conductivity of sulfur limit their development. In this work, the highly conductive $Li_7P_3S_{11}$ glass-ceramic solid electrolyte with room temperature conductivity of 1.27 mS cm^{-1} is synthesized and combined with the FeS_2 cathode and Li-In anode to fabricate $FeS_2/Li_7P_3S_{11}/Li$-In all-solid-state Li-S battery. The assembled battery delivers high initial discharge capacities of 620.8, 866.4 mAh g^{-1}, and 364.8 mAh g^{-1} at 0.1C under room temperature, 60°C and 0°C, respectively. It shows a discharge capacity of 284.8 mAh g^{-1} with a capacity retention of 52.4% after 80 cycles at room temperature. When the operating temperature rises to 60°C, this battery suffers a fast decay of capacity in 40 cycles. However, this battery sustains a high discharge capacity of 256.6 mAh g^{-1} with a capacity retention of 87.9% after 100 cycles under 0°C, smaller volume expansion of ASSBs at 0°C keep the solid/solid contact between the electrolyte particles, thus resulting in better electrochemical performances. EIS and *in situ* pressure characterizations further verify that the differences of electrochemical performances are associated with the volume variations caused by the temperature effects. This work provides a guideline for designing all-solid-state Li-S which is workable in a wide temperature range.

KEYWORDS

all-solid-state Li-S batteries, Li7P3S11 solid electrolyte, temperature effect, electrochemical performances, volume variations

Introduction

Large scale stationary energy storage, as well as the development of hybrid cars for the ground and the air, need for the use of sophisticated secondary batteries with high energy density, high specific energy, extended cycle lives, high safety standards, and low cost. However, due to their intrinsic limits, currently available secondary batteries such as intercalation-type Li ion batteries (LIBs), lead acid batteries, and nickel metal hydride

batteries are unable to meet all these criteria at the same time. (Bruce et al., 2011; Yang et al., 2011; Zhang, 2015; Seh et al., 2016; Yuan et al., 2016; Chen et al., 2018; Liu et al., 2018; Yuan et al., 2020). Li-sulfur (Li-S) batteries are considered as one of the most promising alternatives for large-scale energy storage systems due to their potential high specific energy (over 900 Wh kg^{-1}) by employing low-cost sulfur and high theoretical specific capacity Li as cathode/anode materials, respectively. (Kolosnitsyn and Karaseva, 2008; Yang et al., 2014; Ulissi et al., 2018; Zhang et al., 2019). However, several fundamental issues and industrial obstacles, such as the poor electronic conductivity of S, the shuttle effect of Li polysulfide, and the huge volume expansion of S during cycling limits its wide applications. One solution to address the above problems is to replace the liquid electrolytes with non-flammability inorganic solid electrolytes to construct all-solid-state Li-S batteries with enhanced safety. Moreover, the new work mechanism in solid-state battery avoids the formation of Li polysulfide and the shuttle effect. Solid electrolytes exhibit more stable Li stripping and plating due to the larger Young's modulus, enabling to utilize lithium metal anode to fabricate solid-state lithium metal batteries with higher energy densities. (Wang et al., 2010; Son et al., 2014; Wang et al., 2014; Zhao et al., 2014; Gallardo et al., 2016; Zhu et al., 2016; Descostes et al., 2020).

Solid electrolytes, as the crucial component of solid-state battery, exert great impact on battery performance, sulfide solid-state electrolytes have advantageous properties for application in Li-S all-solid-state batteries, including high Li^+ conductivity ($10^{-3} \sim 10^{-2}$ S cm^{-1}) and low interfacial resistance between the electrode and electrolyte. (Pang et al., 2021; Wu et al., 2021; Liao et al., 2022a; Peng et al., 2022). Many sulfide electrolytes have been successfully developed for all-solid-state batteries. (Guo et al., 2022; Lin et al., 2022; Liu et al., 2022; Zeng et al., 2022). Compared with most of other SSEs, $Li_7P_3S_{11}$ achieved a much higher experimental ion conductivity of around 1.7×10^{-2} S cm^{-1}, a theoretical conductivity of around 7.2×10^{-2} S cm^{-1}, and lower activation energy of around 12 kJ mol^{-1} at room temperature. (Hayashi et al., 2010; Wan et al., 2019). It also shows more favorable kinetic stability on the interface between electrodes and SSEs, making it one of the best SSEs for ALSSBs.

High-energy-density conversional-type electrode materials such as FeS_2, Li_2S, have recently drawn attention due to the progress of Li metal and solid electrolytes. FeS_2 is an abundant and inexpensive natural material with a high theoretical capacity of up to 894 mAh g^{-1} based on the complete conversion from FeS_2 to Li_2S and Fe. Therefore, FeS_2 has been considered a promising high-capacity cathode material for lithium batteries. The shuttle effect of polysulfides, large volume variations throughout the cycling process, and irreversible loss of active ingredients are still the significant obstacles. (Cheng et al., 2016; Zhang and Tran, 2016). The

primary problem is the enormous volume fluctuation that occurs throughout the Li^+ plating/stripping process (159.2%), which results in worse contraction between cathode materials and electrolyte. (Wang et al., 2010; Wang et al., 2019). Therefore, overcoming the volume expansion is the basis for the FeS_2 cathode materials' practical application.

In addition, temperature effect has a significant impact on electrochemical performance. Higher ionic conductivity can be achieved at high temperatures and lower temperatures result in a lower ionic conductivity of solid electrolytes. Moreover, the lithium-ion migration kinetics and side reaction of the electrode/electrolyte solid interface, are also influenced by the operating temperatures. (Peng et al., 2021). Moreover, as to the liquid-state lithium–sulfur batteries, the fluidity electrolytes can build ionic conducting connections between different parts. While the three-dimensional conducting framework in solid-state Li-S batteries is based on various types of solid-solid connections, leading to more severe volume variations of solid/solid contacts during cycling, especially under different operating temperatures. (Rodrigues et al., 2017; Choi et al., 2018). However, the evaluations of solid/solid contacts and electrochemical performances of $Li_7P_3S_{11}$-based solid-state Li-S batteries operated at different temperatures are unclear. Revealing those working mechanisms is vital to constructing high-performance all-climate solid-state Li-S batteries.

In this work, the $Li_7P_3S_{11}$ are employed as solid electrolytes to construct SSBs combined with pristine FeS_2 and Li–In anode. Systematical investigations have been performed to unravel the temperature influence of FeS_2 cathode on electrochemical performances of the assembled $Li_7P_3S_{11}$-based SSBs. *In-situ* stack pressure measurement, *in situ* EIS and DRT are used to investigate the stress variations and monitor the resistance evolution in solid-state batteries under various operation temperatures of solid-state batteries, the effect of temperature effect are unraveled, indicating that the phase transformation and the volume effect exert great impact to the battery performance, and highly affected by ambient temperature.

Experimental procedures

$Li_7P_3S_{11}$ electrolyte was prepared *via* mechanical milling method of the appropriate stoichiometry ratio of the Li_2S (Sigma Aldrich, 99.98%), P_2S_5 (Macklin, 99%), employing a planetary ball mill (Retsch, PM 200) for 15 h at 500 rpm within a ZrO_2-coated stainless steel jar. The prepared amorphous glass mixture was annealed at 270°C for 3 h to obtain the $Li_7P_3S_{11}$ electrolytes. The cathode mixture $FeS_2@Li_7P_3S_{11}@C$ was obtained by blending FeS_2 with C (CNTs) and $Li_7P_3S_{11}$ with a weight ratio of 4:5:1. The mixing process was achieved by the ball milling method. The above synthesis process was carried out under an Ar atmosphere in the glove box to avoid air reacting with solid-state electrolytes.
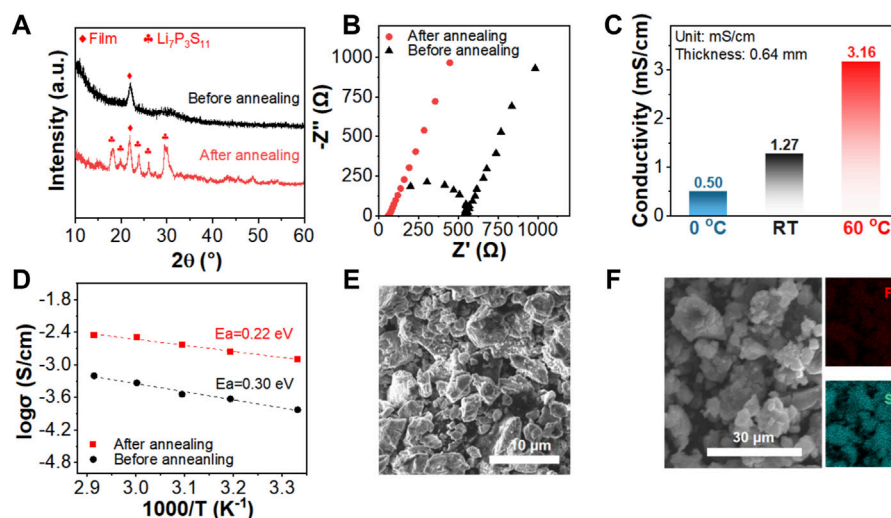
FIGURE 1
(A) XRD patterns of $Li_7P_3S_{11}$ before and after annealing, **(B)** the complex Nyquist plots of the $Li_7P_3S_{11}$ before and after annealing, **(C)** the corresponding Li-ion conductivity of the prepared $Li_7P_3S_{11}$ measured at different temperatures (0°C, RT and 60°C). **(D)** The corresponding Arrhenius plots of $Li_7P_3S_{11}$ before and after annealing, **(E)** SEM images and **(F)** the EDS mapping images of the sintered $Li_7P_3S_{11}$ electrolytes.

XRD patterns of the solid-state electrolyte $Li_7P_3S_{11}$ were collected from a SmartLab-SE Powder instrument with a 2θ ranging from 10° to 80° using Cu Kα radiation. Morphology and EDS mappings of solid-state electrolytes were observed by SEM (Hitachi S-4800 II FESEM). Ionic conductivities were measured *via* pelletizing 100 mg of electrolytes into a pellet with a 10 mm diameter and using mold cells. An impedance analyzer (Solartron, 1,260) with an amplitude of 10 mV was utilized to obtain the impedance spectrum.

To fabricate $FeS_2/Li_7P_3S_{11}/Li$-In solid-state battery, 3 mg of cathode mixture and 80 mg of solid electrolytes were pressed into a bilayer pellet under 380 MPa. Then, the Li-In anode was placed on another side of the electrolytes and pelletized under 150 MPa to form the solid-state battery. The mass loading for the solid-state batteries was fixed at 3 mg. Galvanostatic charge-discharge measurements were performed under different densities between 0.6 and 2.4 V vs. Li-In and under different temperatures (0°C, room temperature, and 60 C) by a charge/discharge device from Neware (CT4008). Cycling voltammetry curves were obtained from an electrochemical workstation (Solartron, 1470E) at a scan rate of 0.2, 0.4, 0.6, 0.8 and 1.0 mV/s. The *in situ*/*ex-situ* EIS measurements were conducted with a Bio-Logic SP-300 in the frequency range of 0.1 Hz–6 MHz with an applied voltage of 0.02 V.

Result and discussions

$Li_7P_3S_{11}$ was chosen as the solid electrolyte in combination of the FeS_2 cathode and Li-In anode in this work to fabricate all-solid-state Li-S batteries. To prepare the target $Li_7P_3S_{11}$ glass-ceramics solid electrolyte, the typical mechanical milling followed by sintering process was applied. As shown in Figure 1A, the XRD pattern of the raw material mixture after high-rotation process exhibits a typical halo-pattern structure, indicating the formation of an amorphous phase. After a subsequent annealing process at 270°C, the major diffraction peaks are indexed to a pure $Li_7P_3S_{11}$ phase with a space group of *P1*. AC impedance was performed on both samples using the stainless steel as the blocking electrodes. The XRD patterns and SEM figures of the synthesized $FeS_2@Li_7P_3S_{11}$ cathode materials are shown in Supplementary Figure S1. The $Li_7P_3S_{11}$ glass-ceramic solid electrolyte was obtained by annealing the high-rotation speed milled processor and thus show poor crystallinity. To achieve a good solid-solid interfacial contact of the $Li_7P_3S_{11}$-FeS_2 cathode mixture, a high milling speeds was applied to mill for a long duration. Therefore, the diffraction peaks due to the $Li_7P_3S_{11}$ electrolyte are unobvious in the obtained cathode mixture. While for the FeS_2 cathode with good crystallinity, it shows strong diffraction peaks in the pattern. As shown in Figures 1B,C the total resistance of the milled mixture is 554.6 Ω, while it lowers to 60.9 Ω for the obtained $Li_7P_3S_{11}$ glass-ceramics after annealing at 270°C for 3 h. The corresponding room temperature Li-ion conductivities are 0.14 and 1.27 mS cm^{-1}, respectively. Besides the ultrahigh conductivity at room temperature, the obtained $Li_7P_3S_{11}$ electrolyte delivers conductivities of 3.16 mS cm^{-1} and 0.50 mS cm^{-1} at 60°C and 0°C, respectively. The activation energy can be deduced based on temperature-dependent ionic conductivities. As shown in Figure 1D the milled mixture shows an E_a of 0.30 eV, while
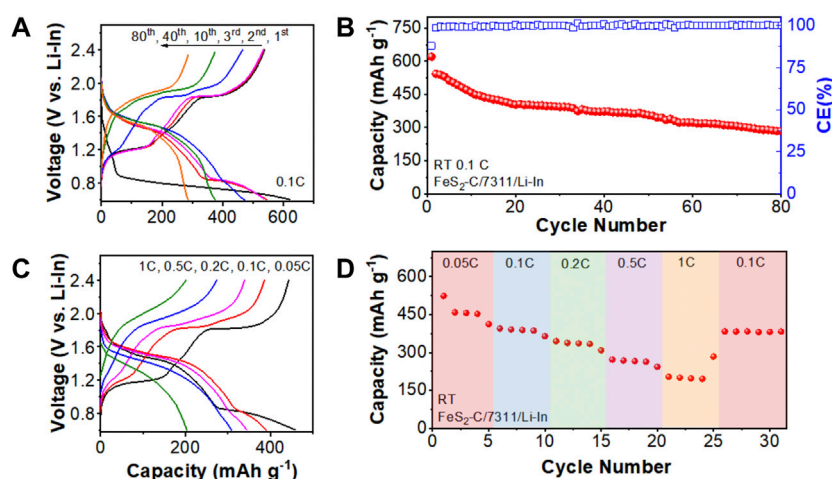
FIGURE 2
(A) The charge/discharge curves and **(B)** the corresponding cycling performances of the assembled $FeS_2/Li_7P_3S_{11}/Li$-In solid-state batteries cycled at 0.1C. **(C)** The charge/discharge profiles of the above battery cycled at different C-rates and **(D)** the rate capability test results. All measurements were performed at room temperature.

the sintered $Li_7P_3S_{11}$ glass-ceramics delivers a much smaller E_a of 0.22 eV. The precursor obtained by the mechanical milling process is a glass phase. A subsequent sintering process is applied to prepare the final $Li_7P_3S_{11}$ glass-ceramic solid electrolyte with a higher Li-ion conductivity due to the improved crystallinity of the material. The increase in conductivity and decrease of activation energy is due to the variation of crystal structure, which widens the transporting path of lithium ions. (Peng et al., 2021). SEM image in Figure 1E shows that the particle size of the prepared $Li_7P_3S_{11}$ glass-ceramic is 5–8 μm with homogenous distribution of P and S in the structure based on the EDS mapping result (Figure 1F).

All-solid-state Li-S batteries consisting of the FeS_2 cathode, the prepared $Li_7P_3S_{11}$ solid electrolyte, and the Li-In alloy anode were constructed and cycled at different charge/discharge C-rates between 0.6 V and 2.4 V (vs. Li-In). Figure 2A shows the charge/discharge profiles of the chosen 1st, 40th, and 80th cycles when the assembled battery cycled at 0.1C under room temperature and the GITT plots of the assembled batteries are shown in Supplementary Figure S2. During the initial discharge process, the battery delivers two discharge plateaus of ~1.3 and ~0.8 V (vs. Li-In) with a discharge capacity of 620.8 mAh g^{-1}. This lower voltage plateau agrees well with the initial discharge plateau (~1.4 V vs Li^+/Li^o) of the lithium batteries using organic liquid electrolytes. (Xu et al., 2018). This initial discharge process with two discharge plateaus reflects the 4-electron reactions from the starting FeS_2 active electrode material to Fe and Li_2S. (Zhou et al., 2020). During the following initial charge process, two charge plateaus located at ~1.2 and ~1.8 V (vs Li-In) are observed in the profile. The lower charge plateau represents the electrochemical reaction between Fe and Li_2S to form the FeS and Li, resulting in a

theoretical voltage of 1.7 V (vs Li^+/Li^o). (Sun et al., 2020). This value agrees well with the first charge plateau voltage of ~1.2 V vs Li-In (~1.8 V vs. Li^+/Li^o). While the higher charge plateau reflects the oxidation of the remaining Li_2S to S with a theoretical voltage of ~2.3 V (vs. Li^+/Li^o), which is in good agreement with the other charge plateau observed in the profile at ~1.8 V vs. Li-In (~2.4 V vs. Li^+/Li^o). (Mwizerwa et al., 2020). After 80 cycles, the assembled battery sustains a discharge capacity of 284.8 mAh g^{-1} with a capacity retention of 52.4% based on the second discharge capacity (Figure 2B). Based on previous literatures, the conversion-type electrode materials suffer severe capacity degradation during cycling even with organic liquid electrolytes due to the large volume expansions. (Son et al., 2014). This situation becomes even worse when it combines $Li_7P_3S_{11}$ solid electrolytes in all-solid-state batteries, the effective solid-solid interfaces between different compounds in the electrode mixture are destroyed due to the volume expansion, yielding large interfacial resistances and poor cycling performance for the assembled all-solid-state Li-S batteries. Besides, the rate capability of the assembled battery was also validated at different charge/discharge C-rates. In Figure 2C, at a low charge/discharge rate, the platforms are caused by the two-step reaction with $FeS_2 \rightarrow FeS + Li_2S \rightarrow Fe + Li_2S$, accompanied by two plateaus at 1.5 V and 0.8 V (vs Li-In), respectively. In contrast, the plateau represents the one-step reaction ($FeS_2 \rightarrow Fe + Li_2S$) at a high rate (such as 1C). As shown in Figure 2D, the $FeS_2/Li_7P_3S_{11}/Li$-In battery delivers discharge capacities of 591.5 mAh g^{-1} at 0.05C, 587.6 mAh g^{-1} at 0.1C, 542.3 mAh g^{-1} at 0.2C, 417.8 mAh g^{-1} at 0.5C, and 313.6 mAh g^{-1} at 1^oC, respectively, showing a rate capability retention of 53.0% (for rate ranging from 0.05 to 1C).
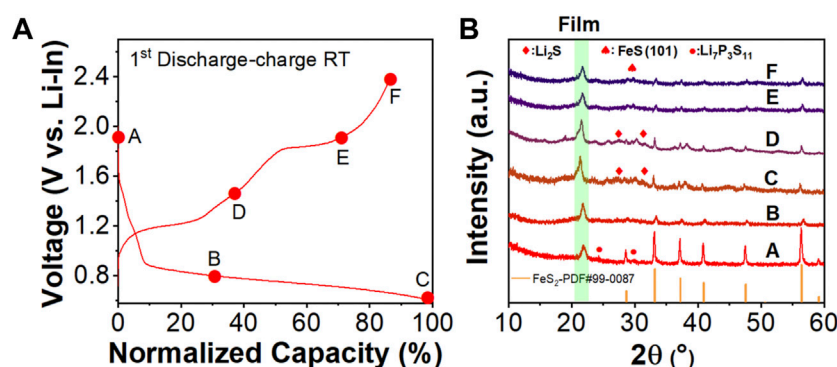
FIGURE 3
(A) The first discharge/charge curves when cycled at room temperature with normalized capacity. The marked A-F are corresponding to various charging/discharging states at different cut-off voltages during cycling. **(B)** The *ex-situ* XRD patterns of the cycled cathode mixtures at different cut-off voltage from A to F. The orange vertical bar represents PDF #99-0087 (Pyrite).

In addition, *ex-situ* XRD was performed on the cycled cathode mixtures of the assembled $FeS_2/Li_7P_3S_{11}/Li$-In batteries after different charge/discharge states to unravel the phase evaluations during the initial cycle. In Figure 3B, the diffraction peak at ~ 21° is assigned to the protective film to isolate the direct contact between the cycled mixture and the air/moisture. As shown in Figure 3B, the diffraction peaks of point A are indexed to the pure phase of the FeS_2 phase at the very beginning of the initial discharge process. It should be mentioned that very weak diffraction peaks due to the $Li_7P_3S_{11}$ solid electrolyte can be detected in this pattern. That's because the electrode mixture was prepared by mixing the crystalline FeS_2 with glass ceramic $Li_7P_3S_{11}$ electrolyte with a high rotation speed up to 500 rpm for long milling durations to ensure good solid-solid interfaces. The $Li_7P_3S_{11}$ electrolyte in the mixture transfers to an amorphous phase after this mechanical milling process, which makes it difficult to be detected by the typical powder XRD. (Prasada Rao et al., 2016). During the discharging process from A to C, the diffraction peaks assigned to the FeS_2 phase become weak because of the reaction between the FeS_2 and Li ions. During this initial discharge process, the XRD peaks indexed to the FeS_2 phase become weaker while the XRD diffraction peaks belonging to the Li_2S and Fe become stronger, which is attributed to the conversion reaction from FeS_2 to Li_2S and Fe. In the subsequent charging process of the first cycle, more diffraction peaks indexed to the Li_2S and FeS phases are detected in the XRD patterns of point C and point D. These peaks almost disappear in the subsequent processes and the FeS phases are observable when the electrode is charged to the high cut-off voltage of 2.4 V (vs Li-In) at point F in Figure 3A, suggesting the phase transformation from the Li_2S/Fe to the FeS. It should be mentioned that no signal belonging to Fe is detected in the XRD pattern. Based on previous research, a spontaneous reaction will occur between Fe and FeS_2 to form the FeS. (Zhou

et al., 2020). Partial of the FeS formed during the charging/discharging processes shows an amorphous phase structure, which makes it difficult to be observed with the typical powder XRD and TEM characterization methods. (Wan et al., 2019). As shown in Figure 3A, a tiny capacity is obtained during the charging process from 1.3 V (Point D) to 1.8 V (vs. Li-In). When the charging voltage rises to point E, the oxidation reaction from Li_2S to S occurs during this process, resulting in decreased Li_2S phase and increased S in the cycled cathode mixture. Therefore, weaker diffraction peaks assigned to the Li_2S phase can be detected in the XRD pattern of point E. When the charging voltage further reaches the upper cut-off voltage (2.4 V vs. Li-In), almost all Li_2S in the cathode mixture has already been transferred to the amorphous S, S_x, and the FeS phases. No diffraction peaks belonging to the S and its analogous can be detected in the XRD pattern of the cathode mixture obtained after the initial charging process (point F) due to the amorphous phase of these yielded products. In the following cycles, the charge/discharge capacities are associated with the lithiation/delithiation reaction of those S, S_x, and FeS complex formed during the first cycle.

In-situ EIS was performed on the $FeS_2/Li_7P_3S_{11}/Li$-In battery during the initial cycle when cycled at room temperature. As shown in Supplementary Figures S4, S5, the battery shows small total resistances at different charge/discharge states under 60°C than that at room temperature during the first cycle. That's why the battery delivers higher initial charge/discharge capacities at 60°C than at room temperature. It also implies that the volume expansions in the cathode mixture at the beginning slightly affect the battery performance. When the operating temperature decreases to 0°C, the battery exhibits the largest total resistances among those different temperatures, yielding the smallest initial charge/discharge capacities. Since the spectra show small changes during cycling, the distribution of
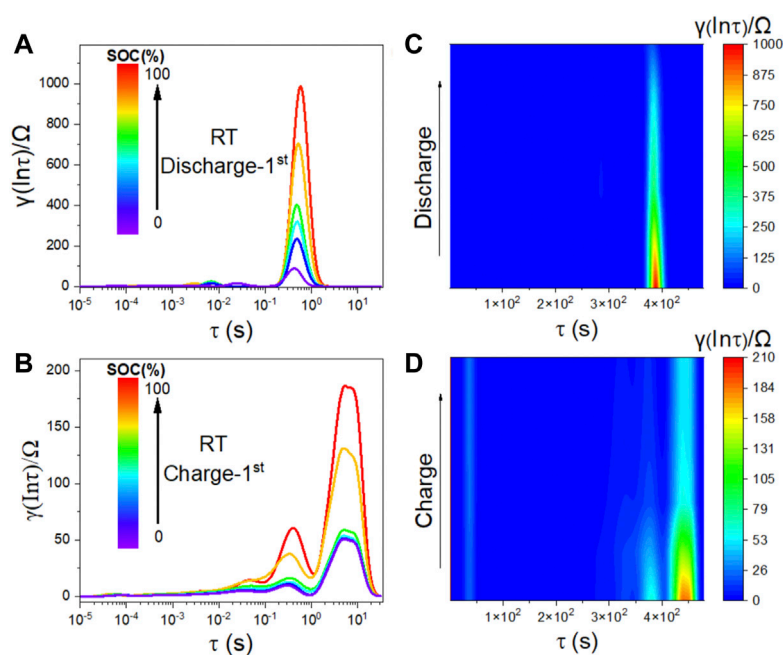
FIGURE 4
The **(A,B)** DRT curves and **(C,D)** obtained based on the *in situ* EIS of the assembled $FeS_2/Li_7P_3S_{11}/Li$-In battery when cycled at 0.1C between 0.6 and 2.4 V (vs. Li-In) under room temperature.

relaxation time (DRT) based on the EIS spectra were applied to unravel the contribution of resistances from different sections of the assembled battery. As depicted in these Figure 4, the peaks centered at $10^{-3}\sim10^{-1}$ Hz is assigned to ion transport across the negative and positive interfaces. The peaks located below 0.1 Hz is related to the solid-state diffusion of Li-ion in FeS_2 in the cathode mixture. Those peaks at 0.1 Hz show clear variations under different discharge states. The intensities first decrease at the beginning of the discharge process and then become stable, reflecting the two lithiation processes of FeS_2 to Li_2S phase in the cathode mixture during cycling. (Li et al., 2022). During the subsequent charging process, obvious peaks are also detected in the DRT figure. The intensity of those peaks centered at $10^{-3}\sim10^{-1}$ Hz increase during the charging process, suggesting a continuous electrochemical reaction associated with the formed Li_2S in the cathode mixture.

Due to the high ionic conductivities of the prepared $Li_7P_3S_{11}$ solid electrolytes at different temperatures, the corresponding electrochemical performances of the assembled $FeS_2/Li_7P_3S_{11}/Li$-In all-solid-state Li-S batteries under these operating temperatures between 0.6 and 2.4 V (vs Li-In) were also investigated. As shown in Figure 5A, the $FeS_2/Li_7P_3S_{11}/Li$-In battery delivers much higher initial discharge and charge capacities of 866.4 mAh g^{-1} than that at room temperature when the battery cycled at 0.1C. Moreover, similar voltage plateaus are observed during the

first charge and discharge processes as that at room temperature. However, it shows much faster discharge capacity decay in the subsequent 40 cycles (Figure 5B). After 40 cycles, the battery only sustains a discharge capacity of 61.8 mAh g^{-1} with a low-capacity retention of 7.1%. The poor cyclability may be associated with the large interfacial resistances of the $FeS_2/Li_7P_3S_{11}/Li$-In battery during cycling when operated at elevated temperatures. One possible reason is the huge volume expansion. (Liao et al., 2022b; Wei et al., 2022b; Wu et al., 2022). As described in the previous section, the FeS_2 electrode materials suffer severe volume expansion at room temperature due to the conversion reaction occurring during cycling. The elevated operating temperatures make this situation even worse. Large volume expansions cause the loss of effective contact between the active material and solid electrolyte particles, yielding lower discharge capacities and poor cycling performances in Figure 5B.

The prepared $Li_7P_3S_{11}$ electrolyte shows a high Li-ion conductivity of 0.50 mS cm^{-1} at 0°C. Considering the huge volume expansions may be mitigated under low operating temperatures, providing a potential application field for this $FeS_2/Li_7P_3S_{11}/Li$-In solid-state battery. As demonstrated in Figure 5C, this battery can reversibly cycle at 0.05C under 0 C for long cycles. It shows almost the same initial discharge and charge curves at this temperature compared to room and elevated temperatures, indicating a similar electrochemical reaction in the
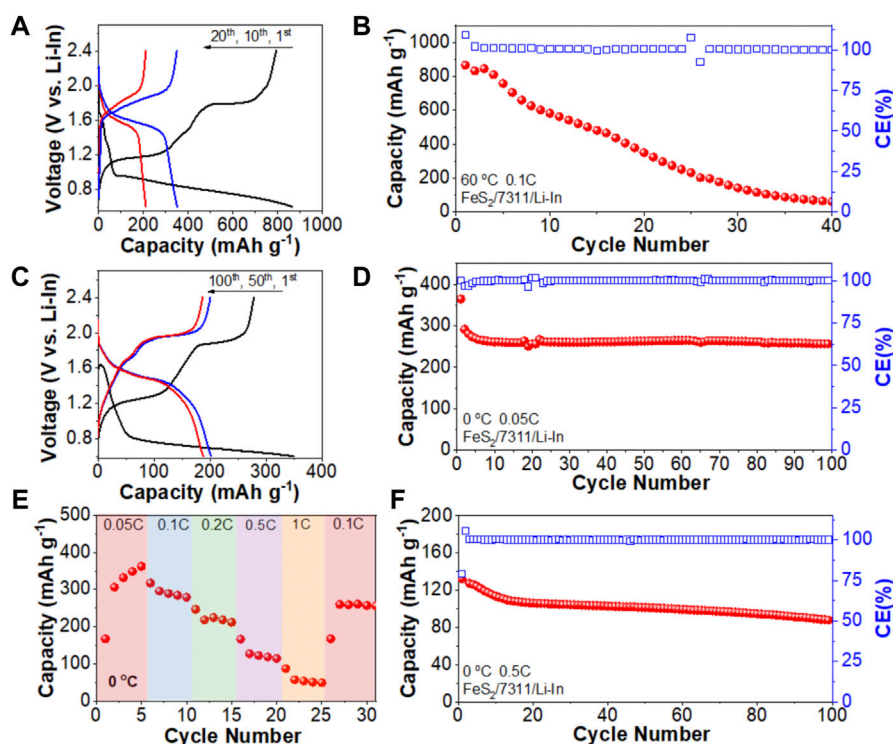
FIGURE 5
(A) The 1st, 10th, and 20th charge/discharge curves and **(B)** the cycling performances of the FeS$_2$/Li$_7$P$_3$S$_{11}$/Li-In battery cycled at 0.1C between 0.6 and 2.4 V (vs. Li-In) under 60°C. **(C)** The 1st, 50th, and 100th charge/discharge plots and **(D)** the cycling performances of the above battery cycled at 0.05°C in the same voltage window under 0°C. **(E)** The rate capability test of the above battery measured at 0°C. **(F)** The cycling performances of the FeS$_2$/Li$_7$P$_3$S$_{11}$/Li-In battery cycled at 0.5C under 0°C. The mass loading of the assembled solid-state battery is 1.53 mg/cm^2.

cathode mixture during cycling. Due to the lower Li-ion conductivity of the Li$_7$P$_3$S$_{11}$ electrolyte at 0°C, the FeS$_2$/Li$_7$P$_3$S$_{11}$/Li-In battery exhibits a much lower discharge capacity of 364.8 mAh g^{-1} under the same test conditions. However, it shows much better cycling performances as depicted in Figure 5D. It sustains a discharge capacity of 256.6 mAh g^{-1} with a capacity retention of 87.9% from 2nd to 100th cycle. Both the capacity and retention values are much higher than that at higher temperatures. As depicted in Figure 5E, it delivers discharge capacities of 458.6 mAh g^{-1} at 0.05C, 390.5 mAh g^{-1} at 0.1C, 335.4 mAh g^{-1} at 0.2C, 265.4 mAh g^{-1} at 0.5C, and 197.2 mAh g^{-1} at 1.0°C, respectively. It shows superior rate capability at this low operating temperature. Finally, this battery was also cycled at a larger C-rate of 0.5C under the same condition. As shown in Figure 5F, it delivers an initial discharge capacity of 132.5 mAh g^{-1} and maintains a discharge capacity of 88.0 mAh g^{-1} with a capacity retention of 69.1% after 100 cycles.

The FeS$_2$ electrode suffers large volume expansions in lithium batteries with the typical organic liquid electrolytes. (Whiteley et al., 2016). Similarly, these volume changes in all-solid-state lithium batteries play an even more crucial role in battery performances. The good solid-solid interface contact ensures

the effective Li-ion transport between different particles in the cathode mixture. (Xi et al., 2019). On the contrary, huge volume variations yield poor solid-solid contacts and large interfacial resistances, resulting in lower capacities and fast capacity decay during cycling. To study the resistance changes of the FeS$_2$/Li$_7$P$_3$S$_{11}$/Li-In battery before and after cycling under different temperatures, EIS was performed. All batteries exhibit an obvious increase in total resistances after cycles. The resistance of the solid electrolyte layer measured in the high frequencies shows minor changes before and after cycling at different operating temperatures based on the EIS spectra in Figures 6A–C, suggesting that the resistances of the solid electrolyte layers of these solid-state lithium batteries stay constant during cycling at various operating temperatures. The major variations of resistance for these batteries come from the interfacial section measured in the middle frequencies. These interfacial resistances increase largely after cycling in Supplementary Figure S3, which may be associated with the huge volume changes from different layers in the solid-state batteries and the conversion reaction of FeS$_2$ in the cathode mixture. (Wei et al., 2022a). The battery cycled at 60°C (Figure 6B) shows the largest increase of interfacial resistance after cycling among those different operating
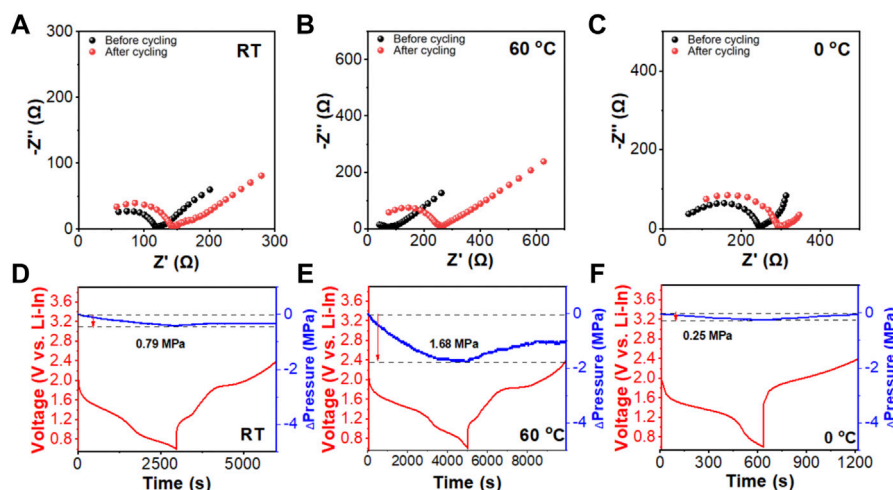
FIGURE 6
The EIS spectra of the assembled $FeS_2/Li_7P_3S_{11}/Li$-In solid-state battery before and after cycling performance tests at different operating temperatures, **(A)** RT, **(B)** 60°C, and **(C)** 0°C. *In-situ* stack pressure evolution plots of the $FeS_2/Li_7P_3S_{11}/Li$-In solid-state battery cycled at 0.5C under **(D)** RT, **(E)** 60°C, and **(F)** 0°C during the first cycling, respectively.
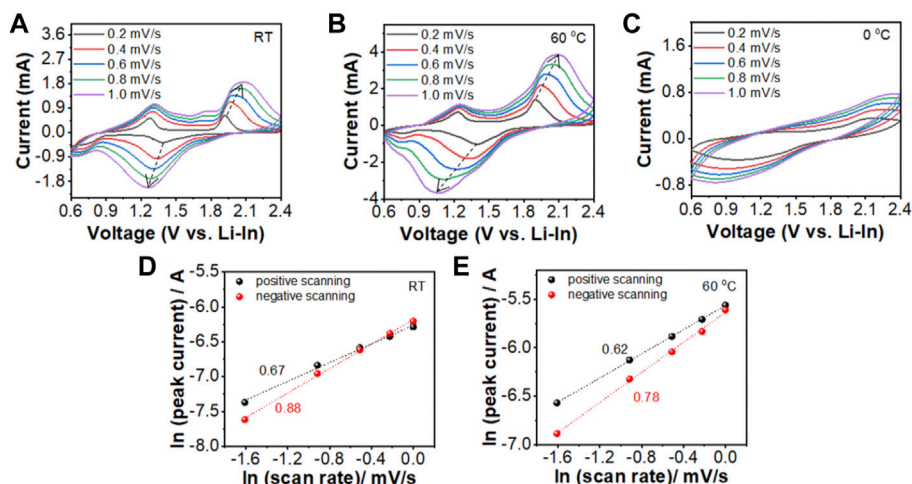

FIGURE 7
CV curves and the corresponding fitting curves of ln (i_p) of the $FeS_2/Li_7P_3S_{11}/Li$-In battery measured with different scan rates at different temperatures **(A,D)** 0°C, **(B,E)** RT, and **(C)** 60°C.

temperatures, which agrees well with the fast degradation of discharge capacities in Figure 5B. While the battery cycled at 0°C (Figure 6C) exhibits the smallest increase of interfacial resistances after 100 cycles, indicating small volume expansions under this temperature. Therefore, the assembled battery shows superior cycling performance at this temperature. At elevated temperatures, the FeS_2 active materials suffer much larger volume expansions during cycling, which destroys the effective solid-solid contact between FeS_2 and $Li_7P_3S_{11}$

electrolyte, resulting in poor cycling performance. When the operating temperature lowers to 0°C, small volume changes are expected due to the shrink effect of materials under cold temperatures. This can maintain effective Li-ion transport across the FeS_2 and $Li_7P_3S_{11}$ solid-solid interfaces, enabling an excellent cycling performance.

In-situ stack pressure tests were performed on the $FeS_2/Li_7P_3S_{11}/Li$-In battery when cycled under the above operating temperatures at 0.5C between 0.6 and 2.4 V (vs Li-In) to monitor

the pressure evolutions in the assembled battery during cycling. As shown in Figure 6, the stack pressure first decreases during the initial discharge processes and increases in the subsequent charge processes. The variation of pressure is associated with the volume expansion and shrinkage of FeS_2 in the cathode mixture during cycling. (Xu et al., 2017). As depicted in Figure D, F, FeS_2/$Li_7P_3S_{11}$/Li-In battery shows the highest (1.68 MPa) and lowest (0.25 MPa) pressure changes when cycled at 60°C and 0°C, respectively, indicating the largest and smallest volume changes under the corresponding temperatures.

These results agree well with our above analysis.

Finally, Cyclic voltammetry (CV) tests under different scan rates were applied to investigate Li-ion mobilities in the cathode mixture of the FeS_2/$Li_7P_3S_{11}$/Li-In battery when worked at different operating temperatures. As shown in Figures 7A–C, similar oxidation/reduction peaks are observed in the CV curves measured at room temperature and 60°C, while no clear peaks can be detected in the CV plots when scanned at 0°C. These results suggest that the battery delivers much higher capacities at elevated temperatures (RT and 60°C) than at low temperatures (0°C). As presented in Figures 7D, E, the FeS_2/$Li_7P_3S_{11}$/Li-In battery shows much higher ln (i_p) values at 60°C than that at RT, suggesting fast Li-ion diffusion rates in the cathode mixture under 60°C. Therefore, the battery delivers much higher charge/discharge capacities at higher temperatures (Figure 5B).

Conclusion

In summary, the pure $Li_7P_3S_{11}$ glass-ceramic electrolyte is successfully synthesized using high-rotation milling followed by a sintering route with a high Li-ion conductivity of 1.27 mS cm^{-1} at room temperature. All-solid-state lithium battery using this prepared $Li_7P_3S_{11}$ electrolyte combined with FeS_2 cathode and Li-In anode delivers a high initial discharge capacity of 620.8 mAh g^{-1} at room temperature when cycled at 0.1C. *Ex-situ* XRD results show that the initial discharge process is associated with the formation of Li_2S from the FeS_2 process, while the following charging process is assigned to the electrochemical reaction of Li_2S. Due to the huge volume expansions that occur at elevated operating temperatures, the assembled FeS_2/$Li_7P_3S_{11}$/Li-In battery delivers a higher initial discharge capacity of 866.4 mAh g^{-1} at 60°C with fast degradation of capacity in the subsequent cycles. Interestingly, although the $Li_7P_3S_{11}$ electrolyte shows a decreased conductivity at a lower temperature, the battery can deliver a high discharge capacity of 364.8 mAh g^{-1} at 0.1C when cycled under 0°C. Moreover, this battery can also show reversible charge/discharge capacity at a higher rate of 0.5C over 100 cycles with excellent cycling performances under the same operating temperature. EIS and *in situ* stack-pressure test results confirm that the superior cycling performance under 0°C and the fast degradation of capacity at 60°C are attributed to the volume changes of FeS_2

in the cathode mixture. This work reveals the temperature effects on the volume changes of solid-state batteries, providing the design principle for constructing high-performance solid-state batteries in a wide temperature range.

Data availability statement

The original contributions presented in the study are included in the article/Supplementary Material, further inquiries can be directed to the corresponding authors.

Author contributions

RW: Conceptualization, Methodology, Data curation, Software. ZW: Conceptualization, Methodology, Data curation, Software. CY: Supervision, Writing—Reviewing and Editing Visualization, Methodology, Resources, Project administration. CW: Formal Analysis. LP: Formal Analysis. LW: Supervision, Writing—Reviewing and Editing Visualization, Methodology. SC: Supervision, Methodology, Resources, Validation. JX: Writing—Reviewing and Editing, Resources, Project administration.

Funding

Acknowledgments

Conflict of interest

The authors declare that the research was conducted in the absence of any commercial or financial relationships that could be construed as a potential conflict of interest.

Publisher's note

All claims expressed in this article are solely those of the authors and do not necessarily represent those of their

affiliated organizations, or those of the publisher, the editors and the reviewers. Any product that may be evaluated in this article, or claim that may be made by its manufacturer, is not guaranteed or endorsed by the publisher.

Supplementary material

The Supplementary Material for this article can be found online at: https://www.frontiersin.org/articles/10.3389/fenrg.2022.1108789/full#supplementary-material

References

Bruce, P., Freunberger, S., Hardwick, J., and Tarascon, M. (2011). Li-O2 and Li-S batteries with high energy storage. *Nat. Mat.* 11, 19–29. doi:10.1038/nmat3191

Chen, L., Li, X., and Xu, Y. (2018). Recent advances of polar transition metal sulfides host materials for advanced lithium-sulfur batteries. *Funct. Mat. Lett.* 11, 1840010. doi:10.1142/s1793604718400106

Cheng, S., Wang, J., Lin, H., Li, W., Qiu, Y., Zheng, Z., et al. (2016). Improved cycling stability of the capping agent-free nanocrystalline FeS2 cathode via an upper cut-off voltage control. *J. Mat. Sci.* 52, 2442–2451. doi:10.1007/s10853-016-0538-8

Choi, S. M. J., Kim, B. K., Sang, B. I., and Kim, H. (2018). Electrochemical behaviors of Li-argyrodite-based all-solid-state batteries under deep-freezing conditions. *Chem. Commun.* 54, 14116–14119. doi:10.1039/c8cc08030e

Descostes, M., Mercier, F., Thromat, N., Beaucaire, C., and Gautier Soyer, M. (2020). Use of XPS in the determination of chemical environment and oxidation state of iron and sulfur samples: Constitution of a data basis in binding energies for Fe and S reference compounds and applications to the evidence of surface species of an oxidized pyrite in a carbonate medium. *Appl. Surf. Sci.* 165, 288–302. doi:10.1016/s0169-4332(00)00443-8

Gallardo, M., Toledo Antonio, J. A., Pal, M., Cortes Jacome, M., and Mathews, N. (2016). Synthesis of pyrite FeS2 nanorods by simple hydrothermal method and its photocatalytic activity. *Chem. Phys. Lett.* 660, 93–98. doi:10.1016/j.cplett.2016.07.046

Guo, Y., Wu, Y., He, Y. B., Kang, F., Chen, L., Li, H., et al. (2022). Solid-state lithium batteries: Safety and prospects. *eScience* 2, 138–163. doi:10.1016/j.esci.2022.02.008

Hayashi, A., Minami, K., Ujiie, S., and Tatsumisago, M. (2010). Preparation and ionic conductivity of Li7P3S11-z glass-ceramic electrolytes. *J. Non. Cryst. Solids* 356, 2670–2673. doi:10.1016/j.jnoncrysol.2010.04.048

Kolosnitsyn, V. S., and Karaseva, E. V. (2008). Lithium-sulfur batteries: Problems and solutions. *Russ. J. Electrochem.* 44, 506–509. doi:10.1134/s1023193508050029

Li, X., Liang, J., Sun, X., Fu, J., Duan, H., Chen, N., et al. (2022). Highly stable halide-electrolyte-based all-solid-state Li–Se batteries. *Adv. Mat.* 34, 2200856. doi:10.1002/adma.202200856

Liao, C., Yu, C., Peng, L., Cheng, S., Xie, J., Zhang, Z., et al. (2022). Achieving superior ionic conductivity of Li6PS5I via introducing LiCl. *Solid State Ionics* 377, 115871. doi:10.1016/j.ssi.2022.115871

Liao, C., Yu, C., Xie, J., Chen, S., Peng, L., Wei, C., et al. (2022). Synthesis of Br-rich argyrodite electrolytes enables all-solid-statebatteries with superior battery performances at different operating temperatures. *Materialia* 26, 101603. doi:10.1016/j.mtla.2022.101603

Lin, J., Chen, S., Li, J., Yu, D., Xu, X. L., Yu, C., et al. (2022). Chlorine-rich lithium argyrodites enables superior performances for solid-state Li–Se batteries at wide temperature range. *Rare Met.* 41, 4065–4074. doi:10.1007/s12598-022-02093-z

Liu, C., Wang, H., Long, T., Ma, Q., Ning, P., Dong, X. R., et al. (2022). Borosilicate glass-enabled antifracture NASICON solid electrolytes for lithium-metal batteries. *ACS Appl. Energy Mat.* 5, 3734–3740. doi:10.1021/acsaem.2c00180

Liu, D., Zhang, C., Zhou, G., Lv, W., Ling, G., Zhi, L., et al. (2018). Catalytic effects in lithium-sulfur batteries: Promoted sulfur transformation and reduced shuttle effect. *Adv. Sci.* 5, 1700270. doi:10.1002/advs.201700270

Mwizerwa, J. P., Zhang, Q., Yao, X., Wan, H., Cai, L., Wang, C., et al. (2020). Sulfur-embedded FeS2 as a high-performance cathode for room temperature all-solid-state lithium-sulfur batteries. *ACS Appl. Mat. Interfaces* 12, 18519–18525. doi:10.1021/acsami.0c01607

Pang, Y., Pan, J., Yang, J., Zheng, S., and Wang, C. (2021). Electrolyte/electrode interfaces in all-solid-state lithium batteries: A Review. *Electrochem. Energy Rev.* 4, 169–193. doi:10.1007/s41918-020-00092-1

Peng, L., Chen, S., Yu, C., Liao, C., Sun, M., Wang, H., et al. (2022). Unraveling the crystallinity on battery performances of chlorine-rich

argyrodite electrolytes. *J. Power Sources* 520, 230890. doi:10.1016/j.jpowsour.2021.230890

Peng, L., Ren, H., Zhang, J., Chen, S., Yu, C., Miao, X., et al. (2021). LiNbO3-coated LiNi0.7Co0.1Mn0.2O2 and chlorine-rich argyrodite enabling high-performance solid-state batteries under different temperatures. *Energy Storage Mater.* 43, 53–61. doi:10.1016/j.ensm.2021.08.028

Prasada Rao, R., Yuen, J. M., and Adams, S. (2016). Rechargeable lithium semi-flow battery using Li7P3S11. *Solid State Ionics* 288, 253–256. doi:10.1016/j.ssi.2016.01.015

Rodrigues, M. F., Babu, G., Gullapalli, H., Kalaga, K., Sayed, F. N., Kato, K., et al. (2017). A materials perspective on Li-ion batteries at extreme temperatures. *Nat. Energy* 2, 17108. doi:10.1038/nenergy.2017.108

Seh, Z., Sun, Y., Zhang, Q., and Cui, Y. (2016). Designing high-energy lithium-sulfur batteries. *Chem. Soc. Rev.* 45, 5605–5634. doi:10.1039/c5cs00410a

Son, S. B., Yersak, T. A., Piper, D. M., Kim, S. C., Kang, C. S., Cho, J. S., et al. (2014). A stabilized PAN-FeS2 cathode with an EC/DEC liquid electrolyte. *Adv. Energy Mat.* 4, 1300961. doi:10.1002/aenm.201300961

Sun, X., Zhu, X., Cao, D., Bruck, A. M., Wang, Y., Zhang, Y., et al. (2020). Operando EDXRD study of all-solid-state lithium batteries coupling thioantimonate superionic conductors with metal sulfide. *Adv. Energy Mat.* 11, 2002861. doi:10.1002/aenm.202002861

Ulissi, U., Ito, S., Hosseini, S., Varzi, A., Aihara, Y., and Passerini, S. (2018). High capacity all-solid-state lithium batteries enabled by pyrite-sulfur composites. *Adv. Energy Mat.* 8, 1801462. doi:10.1002/aenm.201801462

Wan, H., Liu, G., Yao, X., Weng, W., Mwizerwa, J. P., Tian, Z., et al. (2019). Transitional metal catalytic pyrite cathode enables ultrastable four-electron-based all-solid-state lithium batteries. *ACS Nano* 13, 9551–9560. doi:10.1021/acsnano.9b04538

Wang, D., Wang, Q., and Wang, T. (2010). Shape controlled growth of pyrite FeS2 crystallites via a polymer-assisted hydrothermal route. *CrystEngComm* 12, 3797–3805. doi:10.1039/c004266h

Wang, L., Wu, Z., Li, H., Zou, J., Gao, P., Niu, X., et al. (2019). Li-Free cathode materials for high energy density lithium batteries. *Joule* 3, 2086–2102. doi:10.1016/j.joule.2019.07.011

Wang, Y., Qian, X., Zhou, W., Liao, H., and Cheng, S. (2014). Hierarchical nanostructured FeS2 hollow microspheres for lithium-ion batteries. *RSC Adv.* 4, 36597–36602. doi:10.1039/c4ra05600k

Wei, C., Liu, X., Yu, C., Cheng, S., Cheng, S., Xie, J., et al. (2022). Revealing performance of 78Li2S-22P2S5 glass ceramic based solid-state batteries at different operating temperatures. *Chin. Chem. Lett.*, [in press]. doi:10.1016/j.cclet.2022.107859

Wei, C., Yu, C., Peng, L., Zhang, Z., Xu, R., Wu, Z., et al. (2022). Tuning ionic conductivity to enable all-climate solid-state Li–S batteries with superior performances. *Mat. Adv.* 3, 1047–1054. doi:10.1039/d1ma00987g

Whiteley, J., Hafner, S., Han, S., Kim, S. C., Oh, K. H., and Lee, S. H. (2016). FeS2-Imbedded mixed conducting matrix as a solid battery cathode. *Adv. Energy Mat.* 6, 1600495. doi:10.1002/aenm.201600495

Wu, J., Shen, L., Zhang, Z., Liu, G., Wang, Z., Zhou, D., et al. (2021). All-solid-state lithium batteries with sulfide electrolytes and Oxide cathodes. *Electrochem. Energy Rev.* 4, 101–135. doi:10.1007/s41918-020-00081-4

Wu, Z., Chen, S., Yu, C., Wei, C., Peng, L., Wang, H. L., et al. (2022). Engineering high conductive Li7P2S8I via Cl-doping for all-solid-state Li-S batteries workable at different operating temperatures. *Chem. Eng. J.* 442, 136346. doi:10.1016/j.cej.2022.136346

Xi, K., He, D., Harris, C., Wang, Y., Lai, C., Li, H., et al. (2019). Enhanced sulfur transformation by multifunctional FeS2/FeS/S composites for high-volumetric capacity cathodes in Lithium–Sulfur batteries. *Adv. Sci.* 6, 1800815. doi:10.1002/advs.201800815

Xu, X., Liu, J., Liu, Z., Shen, J., Hu, R., Liu, J., et al. (2017). Robust pitaya-structured pyrite as high energy density cathode for high-rate lithium batteries. *ACS Nano* 11, 9033–9040. doi:10.1021/acsnano.7b03530

Xu, X., Meng, Z., Zhu, X., Zhang, S., and Han, W. Q. (2018). Biomass carbon composited FeS2 as cathode materials for high-rate rechargeable lithium-ion battery. *J. Power Sources* 380, 12–17. doi:10.1016/j.jpowsour.2018.01.057

Yang, X., Zhang, L., Zhang, F., Huang, Y., and Chen, Y. (2014). Sulfur-infiltrated graphene-based layered porous carbon cathodes for high-performance lithium-sulfur batteries. *ACS Nano* 8, 5208–5215. doi:10.1021/nn501284q

Yang, Y., Yu, G., Cui, Y., Wu, H., Vosgueritchian, M., Yao, Y., et al. (2011). Improving the performance of lithium-sulfur batteries by conductive polymer coating. *ACS Nano* 5, 9187–9193. doi:10.1021/nn203436j

Yuan, Q., Chen, Y., Li, A., Li, Y., Chen, X., Jia, M., et al. (2020). Polysulfides anchoring and enhanced electrochemical kinetics of 3D flower-like FeS/carbon assembly materials for lithium-sulfur battery. *Appl. Surf. Sci.* 508, 145286. doi:10.1016/j.apsusc.2020.145286

Yuan, Z., Peng, H., Hou, T. Z., Huang, J. Q., Chen, C. M., Wang, D. W., et al. (2016). Powering lithium-sulfur battery performance by propelling polysulfide redox at sulfiphilic hosts. *Nano Lett.* 16, 519–527. doi:10.1021/acs.nanolett.5b04166

Zeng, D., Yao, J., Zhang, L., Xu, R., Wang, S., Yan, X., et al. (2022). Promoting favorable interfacial properties in lithium-based batteries using chlorine-rich sulfide inorganic solid-state electrolytes. *Nat. Commun.* 13, 1909. doi:10.1038/s41467-022-29596-8

Zhang, Q., Cao, D., Ma, Y., Zhu, H., and Aurora, P. (2019). Solid-state batteries: Sulfide-based solid-state electrolytes: Synthesis, stability, and potential for all-solid-state batteries (adv. Mater. 44/2019). *Adv. Mat.* 31, 1970311. doi:10.1002/adma.201970311

Zhang, S. (2015). The redox mechanism of FeS2 in non-aqueous electrolytes for lithium and sodium batteries. *J. Mat. Chem. A Mat.* 3, 7689–7694. doi:10.1039/c5ta00623f

Zhang, S., and Tran, D. T. (2016). Pyrite FeS2 as an efficient adsorbent of lithium polysulphide for improved lithium-sulphur batteries. *J. Mat. Chem. A Mat.* 4, 4371–4374. doi:10.1039/c6ta01214k

Zhao, Z., Wang, S., Liang, R., Li, Z., Shi, Z., and Chen, G. (2014). Graphene-wrapped chromium-MOF(MIL-101)/sulfur composite for performance improvement of high-rate rechargeable Li-S batteries. *J. Mat. Chem. A* 2, 13509–13512. doi:10.1039/c4ta01241k

Zhou, J., Wang, L., Wang, B., Chen, S., Chen, P., Ran, Q., et al. (2020). Unraveling the reaction mechanism of FeS2 as a Li-ion battery cathode. *ACS Appl. Mat. Interfaces* 12, 44850–44857. doi:10.1021/acsami.0c14082

Zhu, Y., Fan, X., Suo, L., Luo, C., Gao, T., and Wang, C. (2016). Electrospun FeS2@carbon fiber electrode as a high energy density cathode for rechargeable lithium batteries. *ACS Nano* 10, 1529–1538. doi:10.1021/acsnano.5b07081